

Article

Charge Storage Mechanism of Li_xWO_3 Hexagonal Tungsten Bronze in Aqueous Electrolytes

Julio César Espinosa-Angeles ^{1,2}, Eric Quarez ¹, Louis-Béni Mvele Eyé'a ¹, Camille Douard ^{1,2}, Antonella Iadecola ², Hui Shao ^{2,3}, Pierre-Louis Taberna ^{2,3}, Patrice Simon ^{2,3}, Olivier Crosnier ^{1,2,*}, and Thierry Brousse ^{1,2,*}

¹ Institut des Matériaux de Nantes Jean Rouxel, IMN, CNRS, Nantes Université, F-44000 Nantes, France

² Réseau sur le Stockage Electrochimique de l'énergie (RS2E), FR CNRS, 3459, F-80039 Amiens, France

³ CIRIMAT, Université Paul Sabatier, F-31062 Toulouse, France

* Correspondence: olivier.crosnier@univ-nantes.fr (O.C.); thierry.brousse@univ-nantes.fr (T.B.)

Abstract: The electrochemical behavior of the lithium hexagonal tungsten bronze, Li_xWO_3 , is investigated herein. The material was synthesized at a low temperature under hydrothermal conditions, yielding nanorod-like particles with growth along the *c*-axis. Upon cycling in a 5 M LiNO_3 aqueous electrolyte, a specific capacity of 71 C.g^{-1} was obtained at 2 mV.s^{-1} , corresponding to a charge/discharge cycle of 10 min. The charge storage mechanism was elucidated using various complementary techniques, such as electrochemical quartz crystal microbalance (EQCM) and synchrotron *operando* X-ray absorption spectroscopy (XAS). A desolvation process upon Li^+ intercalation into the lattice of the material was evidenced, accompanied by a reversible reduction/oxidation of tungsten cations in the crystal structure upon charge/discharge cycling.

Keywords: electrochemical capacitors; tungsten bronze; *operando*; high power electrode; pseudocapacitance; electrochemical quartz crystal microbalance; X-ray absorption spectroscopy



Citation: Espinosa-Angeles, J.C.; Quarez, E.; Mvele Eyé'a, L.-B.; Douard, C.; Iadecola, A.; Shao, H.; Taberna, P.-L.; Simon, P.; Crosnier, O.; Brousse, T. Charge Storage Mechanism of Li_xWO_3 Hexagonal Tungsten Bronze in Aqueous Electrolytes. *Batteries* **2023**, *9*, 136. <https://doi.org/10.3390/batteries9020136>

Academic Editors: Seung-Tae Hong and Junnan Hao

Received: 30 December 2022

Revised: 10 February 2023

Accepted: 11 February 2023

Published: 15 February 2023



Copyright: © 2023 by the authors. Licensee MDPI, Basel, Switzerland. This article is an open access article distributed under the terms and conditions of the Creative Commons Attribution (CC BY) license (<https://creativecommons.org/licenses/by/4.0/>).

1. Introduction

The global drive to make the changeover to greener and safer energy sources has sped up considerably in recent years, as evidenced by the ever-increasing development of renewable technologies such as solar and wind power. These power sources share the inconvenience of only being intermittently available; however, the energy they produce needs to be stored so as to be accessible on demand [1]. Energy storage systems [2], particularly batteries and electrochemical capacitors, may be used to accomplish this objective, although certain challenges remain [3]. While batteries store charge at the bulk of the electrodes through electrochemical redox reactions, in electrochemical capacitors, the charge is stored electrostatically through the adsorption of ions onto the developed surface area of the electrodes. Naturally, these different storage mechanisms lead to distinctive electrochemical properties, such as high energy density as regards the former and high power density for the latter. The holy grail resides in a singular device capable of delivering higher amounts of energy within shorter periods of time, containing an active material that exhibits a fast intercalation mechanism. Dunn [4] and Zukalov [5] reported this particular behavior for TiO_2 , where the charge is stored via the intercalation of lithium ions in a non-aqueous electrolyte displaying a theoretical capacity of 1206 C.g^{-1} (335 mAh.g^{-1}) for a one-electron redox reaction. Additionally, the layered structures of hydrogen titanates, $\text{H}_2\text{Ti}_3\text{O}_7$, were explored due to their pseudocapacitive mechanisms [6,7]. In both of these materials, the redox couple $\text{Ti}^{4+}/\text{Ti}^{3+}$ is responsible for charge storage when the lithium ions intercalate below 2 V vs. Li^+/Li . These investigations were primarily carried out on nanostructured materials, such as nanowires and nanotubes, obtaining a reversible capacity of 597 C.g^{-1} (166 mAh.g^{-1}) in a charge/discharge cycle taking only 5 min [8–12].

Recent reports have served to demonstrate the fast intercalation behavior of orthorhombic T-Nb₂O₅. The charge storage of T-Nb₂O₅ typically occurs due to the intercalation of lithium ions in organic electrolytes at a potential of <2 V vs. Li⁺/Li, with a maximum capacity of 720 C.g⁻¹ (166 mAh.g⁻¹) [13–16]. T-Nb₂O₅, along with TiO₂ and hydrogen titanates, shows a fast intercalation process for Li⁺ in non-aqueous electrolytes. It has been suggested that this behavior is pseudocapacitive in nature; however, one must exercise caution when reporting the values in terms of capacity (C.g⁻¹) as opposed to capacitance (F.g⁻¹) for those materials exhibiting a clear faradaic signature in their CVs [7].

Alternatively, tungsten oxide (WO₃), along with its different polymorphs, is suitable for use in a wide range of applications [17], for instance in photochromic and electrochromic devices [18–21]. Moreover, it has proven to be versatile as an electrode material for batteries and electrochemical capacitors [22]. Augustyn et al. [23,24] reported the pseudocapacitive behavior of the hydrated phase of WO₃•2H₂O: they investigated the fast intercalation of H⁺ in acidic media, which was attributed to the change in oxidation state from W⁶⁺ to W⁵⁺, with a theoretical capacity of up to 360 C.g⁻¹, corresponding to a single electron in the process. This study paves the way for investigating WO₃ as a working electrode in a water-based electrolyte.

Tungsten oxide (WO₃) possesses various polymorphs, the most stable among them being monoclinic I (γ-WO₃) [17], which has been poorly investigated as an electrode material in neutral aqueous electrolyte. However, another possible metastable phase for WO₃ is the hexagonal tungsten bronze (h-WO₃ or HTB). The tungsten bronzes are a widely studied family of compounds with the general formula A_xWO₃, where A is an alkali metal, and x is between 0 and 0.33. Magnéli was the first to report its crystal structure [25], which was confirmed and clarified by Gerand et al. a few decades later [26,27]. The structure was described in terms of the layers of corner-sharing WO₆ octahedra, in the form of three- and six-membered rings in the *ab*-plane. These three- and six-membered rings result in the formation of triangular and hexagonal windows, respectively. Whittingham et al. [28] studied the sodium tungstate phases and were the first to suggest the possibility of the presence of water inside the crystal structure. A few years later, this hypothesis was confirmed by means of a powder neutron diffraction experiment and a Rietveld analysis [29,30]. The electrochemical intercalation of alkali cations was later investigated by Kumagai et al. [31–34]. The hexagonal WO₃ phase was obtained after heat treatment of the orthorhombic hydrated phase at 350 °C; it was shown that it is possible to electrochemically intercalate up to 1.9 Li⁺ into the lattice of h-WO₃ using LiClO₄ in a propylene-carbonate (PC) electrolyte and that this process is reversible. To date, this is the most promising result for a phase of this kind in an organic electrolyte.

We herein propose, for the first time, an electrochemical study of lithium hexagonal tungsten bronze (Li-HTB) under mild aqueous cycling conditions. Additionally, advanced techniques, such as electrochemical quartz crystal microbalance (EQCM) and *operando* X-ray absorption spectroscopy (XAS), were applied in order to shed light on the phenomena taking place not only at the electrode/electrolyte interface of the active material but also further inwards. By virtue of the proposed approach, we are thus able to unveil the charge storage mechanism occurring in Li-HTB and pave the way for future applications of this material in fast aqueous energy storage devices.

2. Materials and Methods

2.1. Hydrothermal Synthesis of Li-HTB

Lithium hexagonal tungsten bronze Li_xWO₃ (Li-HTB) was synthesized in two steps, based on previous studies [20,35–38]. Firstly, 35 mmol of sodium tungstate dihydrate (Na₂WO₄•2H₂O) was mixed with 150 mL of deionized water. Then, 15 mL of concentrated H₂SO₄ was added dropwise under stirring until the formation of a uniform yellow precipitate. This mixture was left under stirring overnight to ensure that all of the WO₃ sol had precipitated. After 24 h, it was washed off with deionized water to remove the remaining acidic solution, and the sol was then mixed with a 0.5 M oxalic acid solution.

The second stage involved hydrothermal synthesis. First, 20 mL of the aforementioned yellow solution was placed in a Teflon-lined vessel, and 2 g of lithium sulfate monohydrate ($\text{Li}_2\text{SO}_4 \cdot \text{H}_2\text{O}$) was then added to it. The vessel was sealed, placed in the appropriate autoclave, and then transferred to an oven where it was heated for 24 h at 180 °C. After the reaction had completed and the autoclave had cooled down, the mixture was washed off with deionized water several times to remove additional side products and then left to dry in air at 80 °C.

2.2. Physico-Chemical Characterization

Li quantification in the Li-HTB compound was carried out through chemical analysis conducted via inductively coupled plasma optical emission spectrometry (ICP-OES), using a Thermo Scientific iCAP 6300 emission spectrometer to analyze the main elements. Thermogravimetric analyses (TGA) were performed in a NETZSCH STA 449 F3 thermal analyzer. The X-Ray diffraction patterns (XRDP) were recorded in air at room temperature (RT) with a Bruker D8 Advance diffractometer using $\text{Cu-K}\alpha 1$ radiation ($\lambda = 1.54060 \text{ \AA}$) and a LynxEye detector in Bragg–Brentano geometry. The structure of the Li-HTB was refined using the JANA2006 program [39]. The morphology and shape of the synthesized particles were characterized using scanning electron microscopy with a Merlin SEM from Carl Zeiss equipped with a 50 mm² X-Max detector from Oxford Instruments NanoAnalysis and transmission electron microscopy with a S/TEM Themis G3 at 300 kV (point-to-point resolution: 0.18 nm). The specific surface area of the powders was determined from the 77 K nitrogen adsorption curves using the BET (Brunauer–Emmett–Teller) method with a Quantachrome Nova 4200e analyzer.

2.3. Electrochemical Characterization and Electrode Preparation

The composite electrodes were prepared by mixing the Li-HTB powder with carbon black, using a PTFE binder, in the respective weight ratios of 60/30/10 as described by Brousse et al. [40] The mixture was suspended in ethanol and heated up to 60 °C under vigorous stirring until complete evaporation of the ethanol. The resulting black slurry was then cooled down and rolled until a composite film with a thickness of between 100 to 150 μm was obtained. After drying at 60 °C to remove the remaining ethanol, it was punched into disks of 10 mm in diameter and pressed at 900 MPa onto stainless steel grids that were used as current collectors. The mass loading of the prepared electrodes varied from 5 to 10 $\text{mg}\cdot\text{cm}^{-2}$, which is in agreement with the assessed properties of electrode materials [41].

The electrochemical performance was evaluated via cyclic voltammetry with a VMP3 galvanostat–potentiostat (BioLogic, EC-Lab software). The experiments were conducted in a three-electrode electrochemical setup using Ag/AgCl (3M NaCl) as the reference electrode and a platinum grid as the counter electrode. A neutral 5M LiNO_3 aqueous solution was used as the electrolyte (pH = 7), and all the experiments were performed in a [−0.6 V; 0 V] vs. Ag/AgCl potential window. This potential window was selected according to results obtained from preliminary electrochemical experiments.

2.4. In-Situ and Operando Setups

2.4.1. Electrochemical Quartz Crystal Microbalance (EQCM)

EQCM sample preparation was performed using BioLogic 1 in.-diameter Ti-coated quartz crystals (resonance frequency, f_0 , 5 MHz) that were spray-coated with a slurry containing 70 wt.% active material, 15 wt.% carbon black, and 15 wt.% polyvinylidene fluoride (PVDF) in N-methyl-2-pyrrolidone (NMP), which was added as a binder. The coated quartz crystal was placed in a PTFE holder before being used as a working electrode, facing the reference electrode (Ag/AgCl). A Pt wire was used as a counter electrode for assembling a three-electrode cell (see Figure S6). Tests were performed in a 5 M LiNO_3 solution serving as the electrolyte (pH = 7). All the EQCM electrochemical measurements

were carried out using a QCM922A from Seiko, combined with an SP200 potentiostat from BioLogic.

2.4.2. X-ray Absorption Spectroscopy

Operando XAS experiments were performed in transmission mode at the ROCK beamline [42] of the SOLEIL synchrotron facility. The XAS spectra were collected at the tungsten L_3 edge (10,204 eV) using a Si (111) quick-XAS monochromator with an oscillation frequency of 2 Hz. The Li-HTB electrodes were placed between the first and second ionization chambers, and a tungsten foil ensured energy calibration. The Li-HTB self-supported electrode was prepared by mixing the active material with conductive carbon, using a PTFE binder, with an average mass loading of $6 \text{ mg}\cdot\text{cm}^{-2}$; 10 mm disks were then pressed in a stainless-steel grid, which had previously been perforated to enable X-ray photon transmission (see Figure S9). A specially designed 3-electrode *operando* cell [43] was used (see Figure S10), with Pt wire as the counter electrode and Ag/AgCl as the reference electrode. Commercially available WO_2 (W^{+4}) and WO_3 (W^{+6}) were used as references to assess the W oxidation state. Firstly, the electrodes were activated using cyclic voltammetry in aqueous 5M LiNO_3 at $20 \text{ mV}\cdot\text{s}^{-1}$ from 0.0 to -0.6 V vs. Ag/AgCl. After a few cycles, the XAS spectra acquisition began with a scan rate of $2 \text{ mV}\cdot\text{s}^{-1}$ in the same potential window. XAS spectra were collected at a frequency of 2 Hz and then averaged 10 by 10 to increase the signal-to-noise ratio, resulting in an averaged spectrum every 5 s (i.e., every 10 mV cycling at $2 \text{ mV}\cdot\text{s}^{-1}$). This procedure allowed us to closely monitor the evolution and changes in the Li-HTB active material in real-time cycling conditions.

3. Results

3.1. Materials Characterization

Hydrothermal synthesis of the Li-HTB resulted in a blueish precipitate attributed to the presence of lithium in the structure, and the hexagonal tungsten bronze phase was thus successfully obtained. To detect and quantify the presence of lithium in the Li-HTB sample, a chemical analysis was carried out using ICP-OES, confirming the amount of 0.16 moles of Li per W atom. Furthermore, thermogravimetric analysis (TGA) showed a gradual mass loss from 100 up to $350 \text{ }^\circ\text{C}$, resulting in a 4% mass loss. The 0.3 moles of H_2O detected can be attributed to water in the crystal structure of the bronze phase (see Figure S1), a fact that will be further confirmed during the structural refinement.

The particles of Li-HTB are defined by growth along the c axis in a spiky nanorod-like shape and stacked on top of one another, as seen in the SEM image (Figure 1A). This morphology is attributed to the interaction of both the Li^+ and SO_4^{2-} ions in the hydrothermal synthesis, which promotes this distinctive type of growth as has previously been demonstrated [20,35–38]. Furthermore, in the TEM image (Figure 1B), the assembly of the initially defined wire particles into broader nanorod-like ones can be seen. Moreover, the electron diffraction pattern inset in Figure 1C confirms the growth of the wires along the c direction, while observing the ab plane from above. Additionally, the BET-specific surface area (SSA), measured according to N_2 adsorption, resulted in $12 \text{ m}^2\cdot\text{g}^{-1}$. This value fits well with the calculated geometric surface area taken up by the nanorods (according to TEM and SEM images), thus indicating that most of the surface is linked to the external surface of the nanorods.

The structural refinement showed that Li-HTB crystallizes in the same space group $\text{P6}/\text{mmm}$ as WO_3 [26], with the cell parameters $a = 7.3328(3) \text{ \AA}$ and $c = 3.86243(18) \text{ \AA}$ and a cell volume of $179.859(12) \text{ \AA}^3$ (Figure S2). The structure of the lithium hexagonal tungsten bronze can be described in terms of the layers of corner-sharing WO_6 octahedra arranged in six-membered rings giving rise to two kinds of tunnels along the c axis, namely, triangular and hexagonal, as shown in Figures S4 and S5. The chemical formula obtained is $\text{Li}_{0.167}\text{WO}_3(\text{H}_2\text{O})_{0.333}$, considering the presence of water molecules in the structure. Moreover, the crystallite size and lattice strain were refined and found to be $54.2(8)$ and $0.379(8) \text{ nm}$, respectively. All additional details are provided in the Supporting Information.

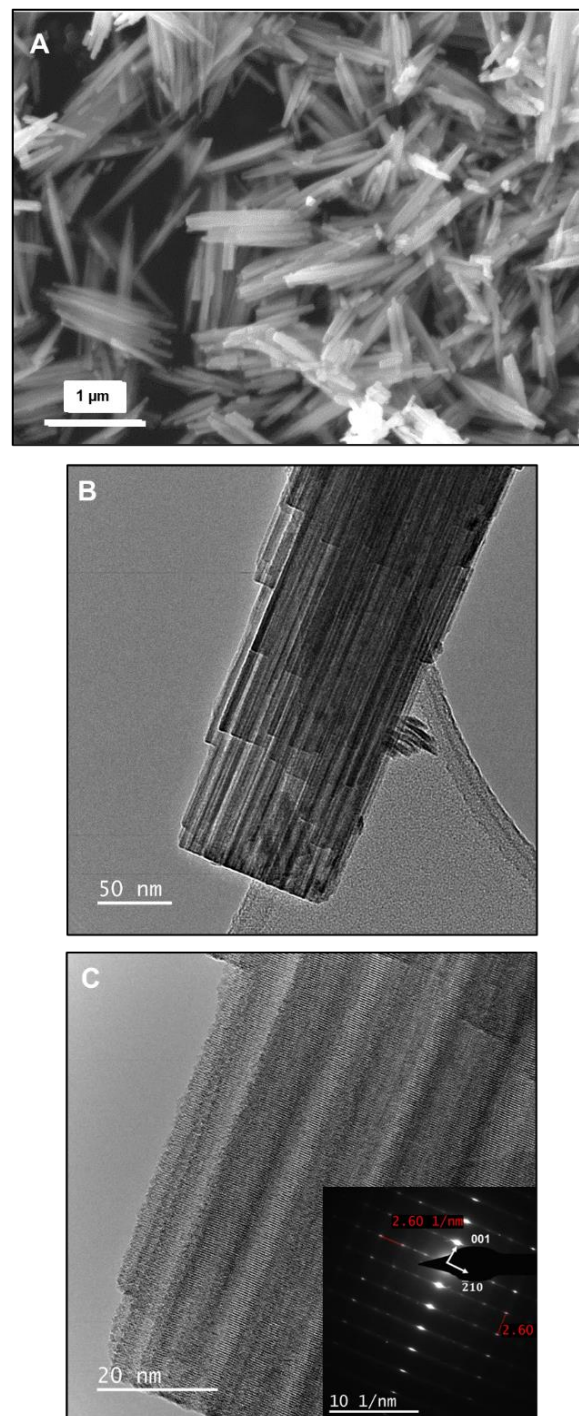


Figure 1. (A) SEM image for the agglomerated spiky nanorods of Li-HTB, (B,C) TEM images of an isolated nanorod, and an inset of the electron diffraction pattern.

3.2. Electrochemical Characterization

The electrochemical behavior of lithium hexagonal tungsten bronze (Li-HTB) operating in an aqueous electrolyte was further evaluated. As shown in Figure 2, the electrochemical signature exhibits faradaic-like behavior with the presence of a reduction peak at -0.43 V vs. Ag/AgCl and the associated oxidation peak at -0.32 V vs. Ag/AgCl during the reverse scan. Furthermore, a quasi-rectangular shape can be perceived when the sweep moves from reduction to oxidation through a small region of the CV. Both the reduction and oxidation peaks are most likely associated with the Li^+ intercalation/deintercalation from

the electrolyte and into the structure of the material. The quasi-rectangular shape described previously is non-diffusion-limited and could be ascribed either to a pseudocapacitive-like behavior [44] caused by fast redox reactions happening at the surface or pure electrostatic storage in the double layer due to ion adsorption onto the surface. Considering the limited surface area of the Li-HTB ($12 \text{ m}^2 \cdot \text{g}^{-1}$), the double layer contribution should be negligible. Indeed, taking into account a double layer capacitance of $20 \text{ } \mu\text{F} \cdot \text{cm}^{-2}$ (which is among the highest commonly indicated values for carbons and metals [45]), this translates into a maximum double layer capacitance of $2.4 \text{ F} \cdot \text{g}^{-1}$, which, in turn, gives a $1.5 \text{ C} \cdot \text{g}^{-1}$ capacity over a 0.6 V potential window, i.e., less than 2 % of the total capacity at $2 \text{ mV} \cdot \text{s}^{-1}$ and only up to 10 % to $100 \text{ mV} \cdot \text{s}^{-1}$.

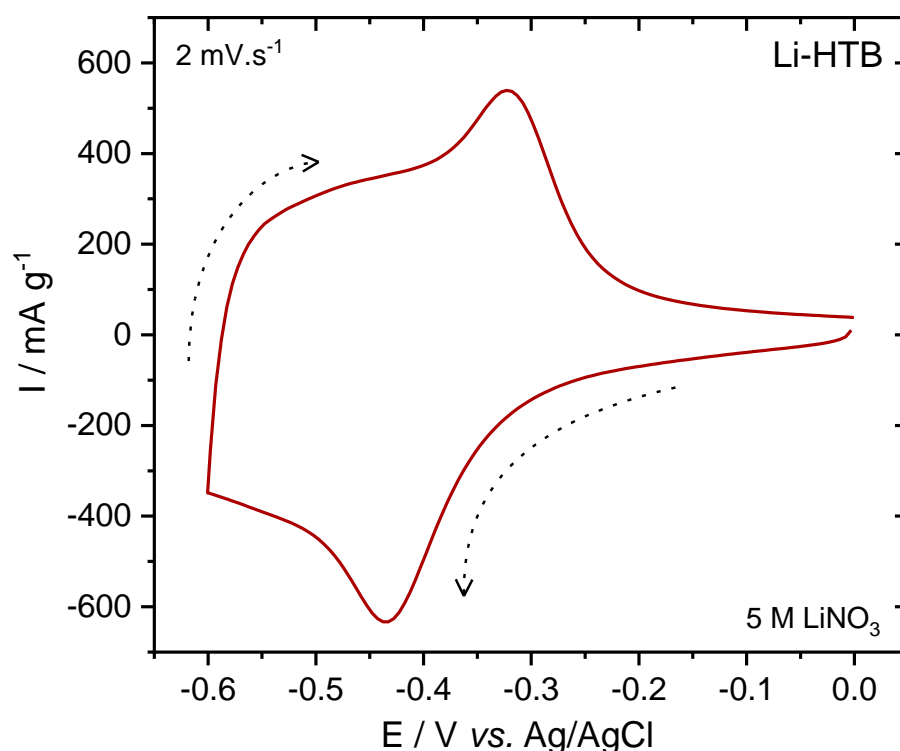


Figure 2. Cyclic voltammogram of Li-HTB at $2 \text{ mV} \cdot \text{s}^{-1}$ in 5M LiNO_3 .

In the CV presented in Figure 2, at a sweep rate of $2 \text{ mV} \cdot \text{s}^{-1}$, a maximum specific capacity of $71 \text{ C} \cdot \text{g}^{-1}$ is achieved, corresponding to a charge/discharge time of 10 min., which is a significantly faster process compared to the charge/discharge rates previously reported for similar compounds in organic electrolytes [32]. Considering that the total theoretical capacity extracted, when one mole of electrons is being transferred, which is about $404 \text{ C} \cdot \text{g}^{-1}$, the number of Li^+ intercalated into Li-HTB at $2 \text{ mV} \cdot \text{s}^{-1}$ works out to be around 0.175 mol per formula unit, as seen in Equation (1):



Figure 3A demonstrates the evolution of the specific capacity as a function of scan rate. Li-HTB reaches above $40 \text{ C} \cdot \text{g}^{-1}$ at $20 \text{ mV} \cdot \text{s}^{-1}$, translating to a charge/discharge rate of only 1 min. Figure 3B displays the CVs corresponding to the evolution of the scan rate from 2 to $100 \text{ mV} \cdot \text{s}^{-1}$. The CVs show how the faradaic response fades when reaching higher sweep rates. At $20 \text{ mV} \cdot \text{s}^{-1}$, a broader anodic peak is still visible, whereas the cathodic peak has disappeared, and the CV shows an increasingly distorted shape, especially as the potential scan direction moves from oxidation to reduction and vice versa (Figure 3B), which is typical of increasing equivalent series resistance. This behavior can be explained kinetically, meaning that the cations in the electrolyte do not have enough time to

intercalate into the material. At higher rates, a non-diffusion-limited surface process takes over. Moreover, whenever the scan rate is further increased, the shape of the CV becomes even more resistive, thereby indicating a certain limitation concerning the interesting intercalation feature described for Li-HTB. Additionally, Figure 3C shows the stability of the Li-HTB at $20 \text{ mV}\cdot\text{s}^{-1}$ over 1000 cycles, even if a slight decay is observed upon the first 400 cycles, presumably due to electrode surface changes that were not unveiled during this study. During the first couple of hundred cycles, there is a slight drop in the capacity, which otherwise remains very stable, even after 500 cycles. As previously mentioned, at $20 \text{ mV}\cdot\text{s}^{-1}$, it is still possible to observe a specific faradaic response in the material.

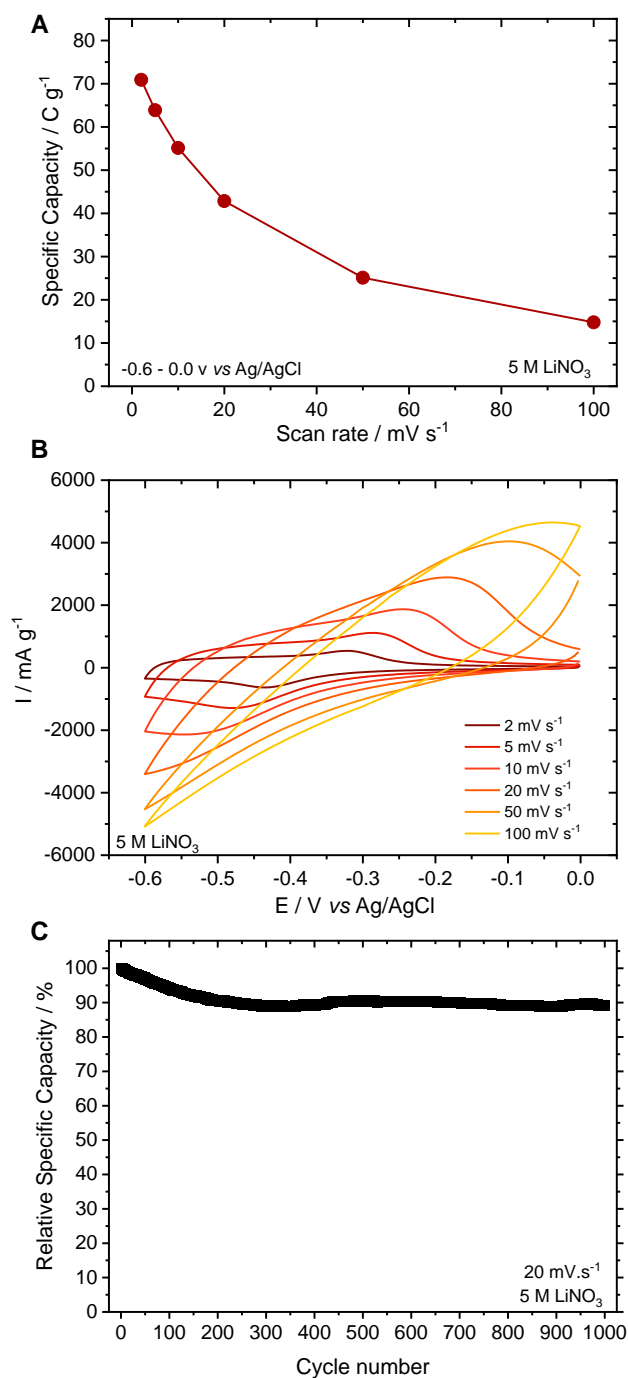


Figure 3. (A) Evolution of the capacity in $\text{C}\cdot\text{g}^{-1}$ vs. the scan rate, (B) cyclic voltammograms of the respective scan rates, and (C) relative specific capacity vs. cycle number. Fluctuations after 400 cycles may be due to slight changes in electrolyte temperature while cycling the electrode.

Li-HTB is capable of accommodating more Li^+ than what is reported here, as previous studies have shown with a similar hexagonal structure although using an organic electrolyte. However, to preserve the structure's stability, a maximum of 0.33 cations can be intercalated [46,47]. Aside from this, it is worth noting that the water occupying the hexagonal cavity between two layers of hexagonal rings (as reported in the structural refinement section, see Figures S2 and S3) might play a role in how the intercalation of Li^+ takes place. In addition, the Li^+ solvation shell should be taken into account, and whether the Li^+ are partially or completely desolvated during the intercalation process needs verifying. This distinctive faradaic behavior serves to highlight certain intriguing features of the lithium hexagonal bronze structure compared to previous reports of hexagonal WO_3 , as well as to the classic $\gamma\text{-WO}_3$. A thorough study of the charge storage mechanism of this compound will be presented in the following section.

3.3. Charge Storage Mechanism Investigation

In order to explain the intercalation mechanism, we performed electrochemical quartz crystal microbalance (EQCM) to monitor the electrode/electrolyte interface (see Figure S6 for the setup).

As the motional resistance is constant, negligible dissipation changes are presumed (see Figures S7 and S8), thereby validating the gravimetric approach and the use of the Sauerbrey's equation (Equation (1)). Figure 4A displays both the CV profile and the frequency response of the Li-HTB phase at $10 \text{ mV}\cdot\text{s}^{-1}$, where the arrows indicate the scan direction. From -0.3 to -0.5 V (vs. Ag/AgCl), an increase in mass is observed, which most likely corresponds to the intercalation of Li^+ into the hexagonal cavities. Figure 4B shows the linear increase in mass versus the accumulated charge (see the orange line). As per Faraday's law, the average molecular weight per charge ($z = 1$) is calculated to be $15.9 \text{ g}\cdot\text{mol}^{-1}$ and could correspond to one mole of Li^+ accompanied by an average of 0.5 moles of H_2O ($\text{Li}^+ \bullet 0.5 \text{ H}_2\text{O}$). This result thus serves to demonstrate that Li^+ cations are not intercalated alone but rather along with the surrounding H_2O molecules. This is in agreement with what has previously been reported for CDCs [48] and MXene [49] phases using aqueous electrolytes.

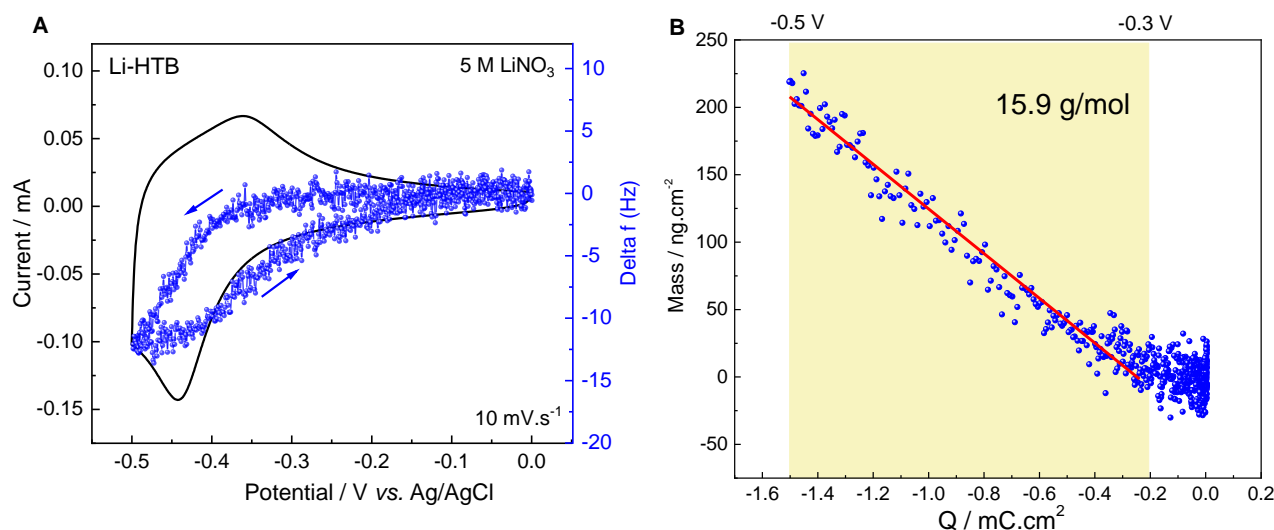


Figure 4. EQCM measurements: (A) CV profile and EQCM frequency response for Li-HTB and (B) electrode mass change versus charge during the polarization in 5 M LiNO_3 , recorded at $10 \text{ mV}\cdot\text{s}^{-1}$ vs. Ag/AgCl as the reference electrode.

Furthermore, X-ray absorption spectroscopy (XAS) was used to directly explore the contribution of tungsten to the charge transfer process. Being a site-selective technique, XAS provides information about both the electronic structure of the absorbing atom (i.e.,

its chemical state) and its local atomic environment (i.e., the bond distances, coordination and geometry) on a very restricted scale (4–5 Å) [50].

Although various in-situ studies exist, only a few contain *operando* analyses performed on materials exhibiting a pseudocapacitive mechanism. An obvious advantage of the *operando* approach is the possibility of observing the changes occurring in real-time, thereby avoiding any parasitic involvement related to relaxation. As the pioneers of this approach, Goubard-Breteshé et al. [43] investigated the behavior of FeWO_4 in aqueous electrolytes, confirming the redox activity of Fe and the spectator role of W. Additionally, Robert et al. [51] notably demonstrated the charge storage process on vanadium nitride films, explaining their high capacitive performance.

Operando XAS was thus our technique of choice for monitoring the W redox activity in the Li-HTB electrode in 5 M LiNO_3 . The W L_3 -edge electronic transition corresponds to the transition of $2p_{3/2}$ electrons towards available 5d states, and the intensity of the peak above the edge, called the white line (WL), is proportional to the 5d empty state. The shift in edge energy is shown in Figure 5, where the normalized absorption in both reduction and oxidation sweeps are displayed. This energy shift to lower values upon reduction is attributed to the decrease in the binding energy of the W absorber core level [52,53], meaning that W is being reduced from W^{6+} to W^{5+} due to the Li^+ intercalation. As indicated by the arrows, the spectra shift towards lower energy values upon reduction and then go back to higher energy values upon oxidation. To precisely assess the W charge transfer upon cycling, these spectra were associated with a respective potential value in the CV of the Li-HTB (Figure 6A), such that each potential value is associated with a specific energy value (Figure 6B). In this way, the shift in energy due to the sweep of potential towards more negative values and then towards more positive values becomes even more apparent.

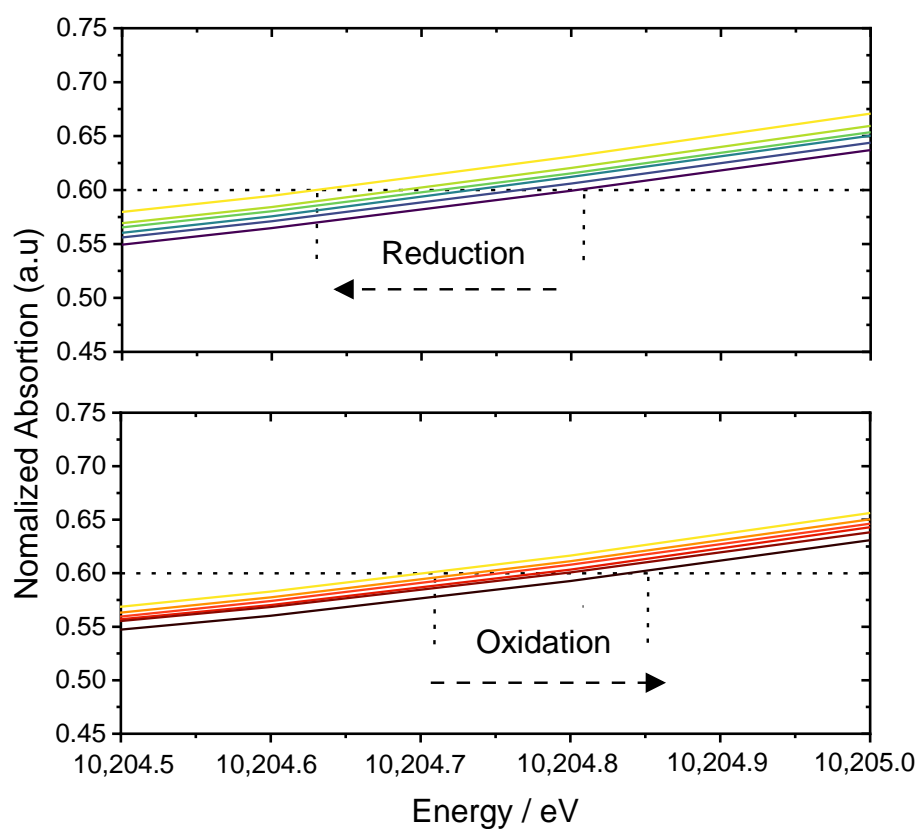


Figure 5. *Operando* XAS for Li-HTB. W L_3 -edge normalized absorption evidencing the changes in energy while cycling the electrodes, upon reduction and oxidation from 0.0 to -0.6 V and back to 0.0 V vs. Ag/AgCl at $2 \text{ mV}\cdot\text{s}^{-1}$.

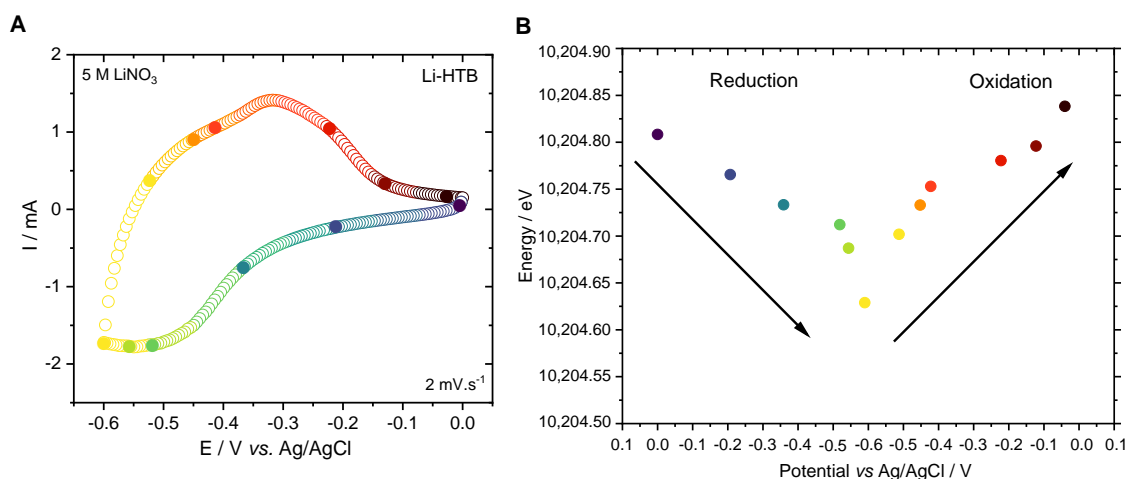


Figure 6. (A) Cyclic voltammogram for Li-HTB at $2 \text{ mV}\cdot\text{s}^{-1}$ in 5 M LiNO_3 (the colored dots represent the XAS spectra acquisition selected for this representation). (B) Evolution of the W L_3 -edge energy position as a function of the sweep of potential vs. Ag/AgCl.

Moreover, this behavior is not linear, as per the findings for the pseudocapacitive materials already reported in [54–56]. Indeed, within a potential window of 0.0 down to -0.4 V vs. Ag/AgCl, the reduction current is steadily increasing, witnessing a pseudocapacitive-like mechanism, while below -0.4 V , a clear intercalation process occurs (Figure 6A). Subsequently, a quicker shift in W L_3 -edge is observed below this potential, leading to a non-linearity in the plot (Figure 6B). This non-linearity indicates that such a mechanism is not entirely pseudocapacitive, and intercalation must be the predominant process at specific values of potential. The same observations are valid upon oxidation scans, where Li^+ de-intercalation is first observed with a rapid increase in W L_3 -edge, followed by a more steady regime.

Figure 7A,B show the electrochemical signature in current vs. time, coupled with the energy shift vs. #scan (spectra number). This representation makes it easier to follow the shift in energy upon cycling, where the energy shift trend is visible when sweeping from more negative to more positive potentials. In order to extract information on the whole dataset, PCA (principal component analysis) and MCR-ALS (multivariate curve resolution–alternating least squares) [57] analyses were performed. Owing to this strategy, we were able to determine how many main components are involved in the electrochemical process when the Li-HTB was being cycled in aqueous 5 M LiNO_3 . Figure 7C displays the concentration profile of the two principal components (blue and red) required to describe the *operando* dataset. Figure 7D shows the reconstructed XANES spectra exhibiting different W oxidation states. Moreover, it is worth noting that, over three cycles, the concentration of the two components is periodic, indicating the good reversibility of the process.

Even though there is very little energy shift upon cycling, the fact that the redox contributions are limited to the interface of the electrode/electrolyte, while the XAS measurements performed in transmission mode are bulk sensitive, should be taken into account. Furthermore, considering the reference samples of WO_2 for W^{4+} and WO_3 for W^{6+} , with an associated energy shift of $\sim 1.0 \text{ eV}$ translated to a difference of $2 e^-$, then it is possible to estimate the number of electrons exchanged by the variation in energy for the Li-HTB. This value was found to be $\sim 0.1 e^-$, which agrees with the value extracted from the capacity obtained during the electrochemical process.

The aforementioned visible faradaic contribution was indeed confirmed by the slight energy shift in the W L_3 -edge position, thereby confirming a slight variation in the oxidation state in the tungsten upon intercalation. Nonetheless, even though we managed to propose a fitting mechanism explaining most of the depicted electrochemical behaviors, there were still a few questions that kept arising whenever the concentration of the electrolyte

changed. We, therefore, decided to investigate these instances, and the corresponding study is presented in the next section.

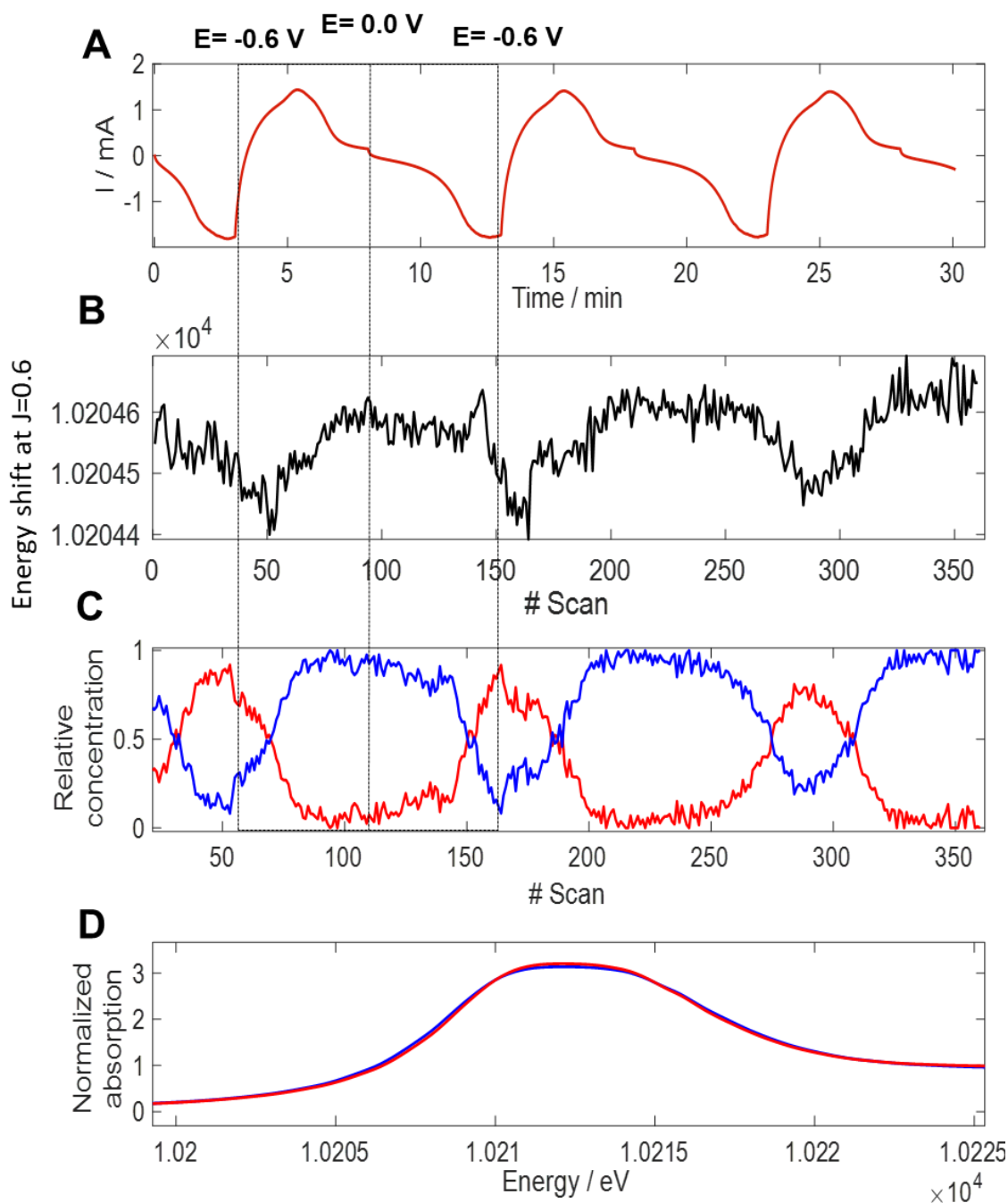


Figure 7. (A) Current vs. time curves for Li HTB. (B) Energy shift obtained at $J = 0.6$ as a function of the spectra number. The dotted lines indicate the values where the potential reaches -0.6 V and goes back to 0.0 V vs. Ag/AgCl. (C) Concentration profile of the two principal components required to describe the *operando* XAS spectra (blue and red). (D) Reconstructed XANES spectra of the two independent components required to describe the Li HTB system.

3.4. Electrochemical Study Using Various Concentrations of LiNO₃

To verify the effect of the salt concentration on the electrochemical signature, an electrochemical study with different LiNO₃ concentrations was performed. Firstly, the number of water moles per Li⁺ moles in each electrolyte tested was determined to find out if there were enough molecules available to form the associated hydration shells. We found

95, 20, and 11 moles of H_2O per 1 mole of Li^+ for 10, 5, and 1 M of LiNO_3 concentration, respectively (see Figure 8A).

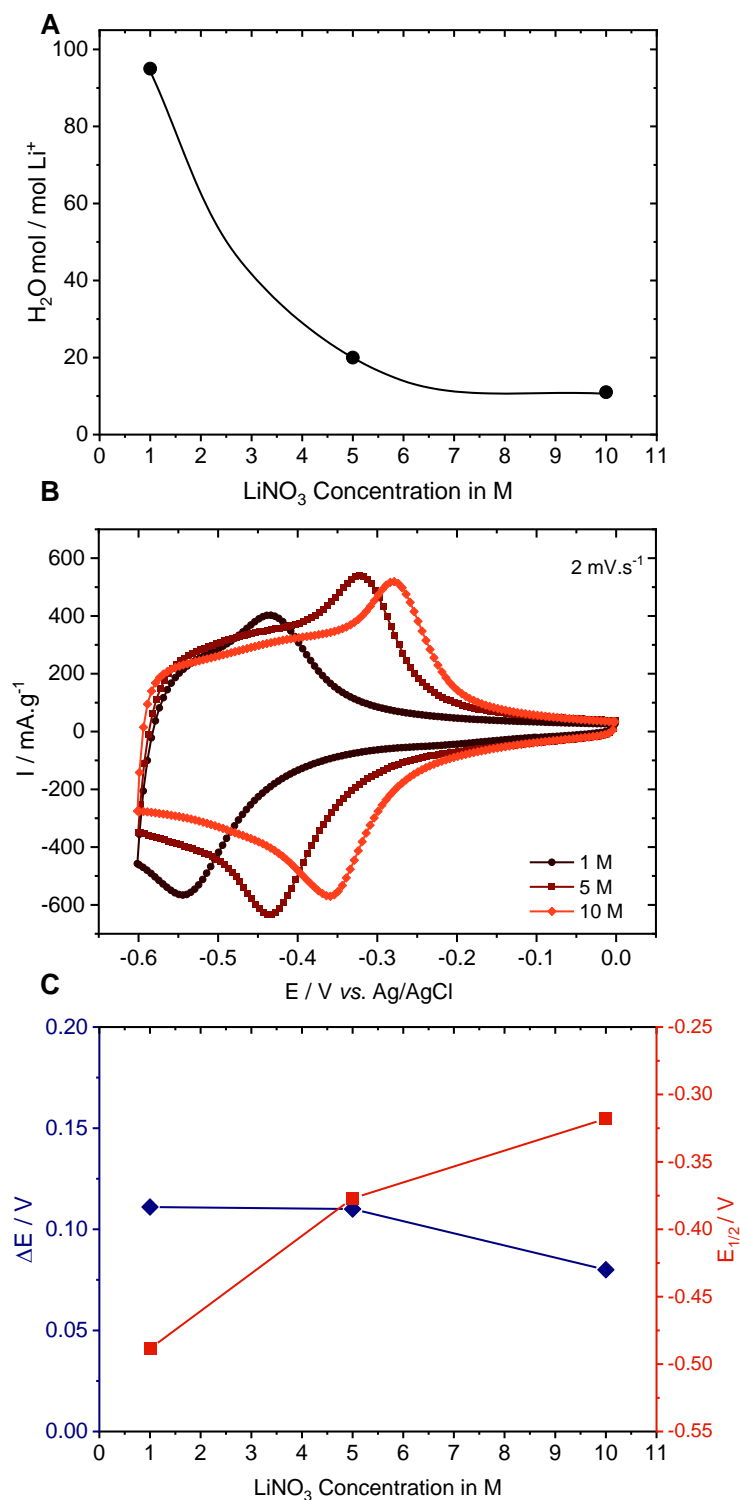


Figure 8. (A) Ratio of moles of H_2O to moles of Li^+ cations vs. electrolyte concentration. (B) Li-HTB cyclic voltammograms in 1, 5, and 10 M aqueous LiNO_3 and (C) ΔE and $E_{1/2}$ vs. electrolyte concentration.

The electrochemical response as a function of the salt concentration is shown in Figure 8B. The CVs display a shift in the peak potentials to positive values when the concentration of Li^+ increases. Moreover, a clear trend linking the concentration and the

potential is observed. The peak potential (cathodic and anodic) separation ΔE and the average potential $E_{1/2}$ (measured by taking the average of the difference between the potential values of anodic and cathodic peaks) vs. the concentration of electrolyte are reported in Figure 8B.

Figure 8C demonstrates that the $E_{1/2}$ moves towards more positive potential values, and the ΔE shrinks as the concentration increases. These changes occurring upon the increase in concentration are probably caused by a decrease in the amount of the energy required for the Li^+ cations to intercalate into the lattice of the materials, thereby facilitating intercalation and making it even more reversible [58]. If less water is available for the Li^+ , then less water is available to form the associated hydration shells (around six water molecules are needed for the first shell) [59–61]. Additionally, according to our conductivity measurements, the conductivity of all the LiNO_3 electrolytes (from 1 to 10 M) is sufficient to provide ions at the desired sweep rate of $2 \text{ mV}\cdot\text{s}^{-1}$. Li^+ cations can thus easily be desolvated, improving their intercalation into the lithium hexagonal tungsten bronze phase. Moreover, the Li^+ intercalation takes place at a more positive potential value (vs. Ag/AgCl) when the ratio of H_2O to Li^+ decreases. Furthermore, the effect observed upon the increase in concentration is merely a result of using a water-based electrolyte and will thus not occur with organic electrolytes, where concentrations as high as those used here cannot be achieved. This, therefore, confirms the fact that the water surrounding the Li^+ plays an important role during Li^+ intercalation into the Li-HTB phase.

4. Conclusions

In this study, Li_xWO_3 hexagonal tungsten bronze (Li-HTB) was synthesized using a low-temperature approach, producing elongated nanorod-like particles. Moreover, the desired crystal structure was obtained, which is formed by assembled layers of corner-sharing WO_6 octahedra arranged in six-membered rings and giving rise to two kinds of tunnels, triangular and hexagonal, along the c axis. This peculiar structure promotes faradaic-like behavior, as evidenced by the redox peaks of its CV, and is due to the intercalation of Li^+ into the water-based electrolyte, resulting in a capacity of $\sim 71 \text{ C}\cdot\text{g}^{-1}$ and a charge/discharge rate of a mere 10 min. Interestingly, the concentration of the electrolyte is strongly correlated to the ability of Li^+ to be desolvated and then intercalated into the lattice of the material. EQCM confirmed that the Li^+ intercalation mechanism is accompanied by around 0.5 moles of H_2O , which is to be expected, considering the half-empty hexagonal cavities that can host some Li^+ in addition to the water molecules surrounding a mole of Li^+ . Furthermore, synchrotron *operando* XAS studies revealed that tungsten is responsible for the charge compensation upon electrochemical cycling. Although the corresponding W energy shift is minute, we were able to successfully identify two main components involved in the electrochemical process using a chemometric approach, based on a combination of PCA and MCR-ALS analyses. To conclude, this study serves to unveil the mechanism involved in Li^+ intercalation into the lattice of Li_xWO_3 , where W is reduced and oxidized in a reversible process. Even though WO_3 is a well-known material, we herein propose an original and low-cost synthesis approach for obtaining Li_xWO_3 possessing a suitable structure and remarkable electrochemical properties for fostering fast energy storage devices in an aqueous electrolyte. Although the performance of such electrode materials are quite modest compared to other materials ($70 \text{ C}\cdot\text{g}^{-1}$ at $2 \text{ mV}\cdot\text{s}^{-1}$), our approach should trigger innovative material engineering taking advantage of the knowledge acquired on lithium hexagonal tungsten bronze.

Supplementary Materials: The following supporting information can be downloaded at: <https://www.mdpi.com/article/10.3390/batteries9020136/s1>, Figure S1: TGA analysis for the Li-HTB sample; Figure S2: Rietveld refinement of $\text{Li}_{0.167}\text{WO}_3(\text{H}_2\text{O})_{0.333}$. The final reliability factors are $R_p = 0.076$, $R_{wp} = 0.100$, $R_{exp} = 0.055$, and $R(F) = 0.046$; Figure S3: Electronic density at $2e(0,0,z)$ with $z \sim 0.30$ (max1) obtained after refining the WO_3 model and performing Fourier difference calculations; Table S1: Atomic coordinates of the $\text{Li}_{0.167}\text{WO}_3$ compound with $a = 7.3328(3) \text{ \AA}$, $c = 3.86243(18) \text{ \AA}$, $V = 179.859(12) \text{ \AA}^3$, and SG $P6/mmm$. Atomic displacement parameters (Å^2),

selected interatomic distances (Å), and bond valence sum calculations; Figure S4: Structure of the $\text{Li}_{0.167}\text{WO}_{3.333}$ compound; Figure S5: (a) O3 atoms in the hexagonal cavity along the *c*-axis and O-O distances and (b) Li-O distances (distances in angstroms); Figure S6: Schematic of EQCM setup; Figure S7: Change of the motional resistance of Li-HTB on a Ti substrate in 5 M LiNO_3 at $10 \text{ mV}\cdot\text{s}^{-1}$; Figure S8: (A) Homogeneously coated quartz and (B) CV of bare quartz vs. CV of coated quartz with Li HTB in 5M LiNO_3 at $10 \text{ mV}\cdot\text{s}^{-1}$; Figure S9: Electrode drawing to be used in an *operando* cell for XAS; Figure S10: *Operando* XAS cell. (A) Scheme of the cell indicating the 3-electrode setup and (B) frontal view of the *operando* cell [26,62–68].

Author Contributions: Conceptualization, J.C.E.-A., O.C. and T.B.; methodology, J.C.E.-A., P.S., P.-L.T., O.C. and T.B.; validation, J.C.E.-A., P.S., P.-L.T., O.C. and T.B.; formal analysis, J.C.E.-A., E.Q., L.-B.M.E., C.D., A.I., H.S. and O.C.; investigation, J.C.E.-A., E.Q., L.-B.M.E., C.D., A.I. and H.S.; writing—original draft preparation, J.C.E.-A., E.Q., A.I., H.S., P.-L.T., P.S., O.C. and T.B.; writing—review and editing, J.C.E.-A., O.C. and T.B.; supervision, O.C. and T.B.; funding acquisition, T.B. All authors have read and agreed to the published version of the manuscript.

Funding: This research was funded by the French National Research Agency within the framework of Labex STORE-EX (ANR-10-LABX-76-01).

Data Availability Statement: Not applicable.

Acknowledgments: J.C.E.A. wants to thank Institut des Matériaux de Nantes Jean Rouxel and Nantes Université for financial support. Marion Allart is also thanked for her assistance with the microEDX/WDX analysis and SEM observations. E. Le Calvez is also greatly acknowledged for his pertinent advice. The CIMEN Electron Microscopy Center in Nantes is greatly acknowledged (funded by the French Contrat Plan État-Région and the European Regional Development Fund of Pays de la Loire).

Conflicts of Interest: The authors declare no conflict of interest.

References

1. Dunn, B.; Kamath, H.; Tarascon, J.-M. Electrical Energy Storage for the Grid: A Battery of Choices. *Science* **2011**, *334*, 928–935. [[CrossRef](#)] [[PubMed](#)]
2. Simon, P.; Gogotsi, Y. Perspectives for Electrochemical Capacitors and Related Devices. *Nat. Mater.* **2020**, *19*, 1151–1163. [[CrossRef](#)] [[PubMed](#)]
3. Tarascon, J.-M.; Armand, M. Issues and Challenges Facing Rechargeable Lithium Batteries. *Nature* **2001**, *414*, 359–367. [[CrossRef](#)] [[PubMed](#)]
4. Wang, J.; Polleux, J.; Lim, J.; Dunn, B. Pseudocapacitive Contributions to Electrochemical Energy Storage in TiO_2 (Anatase) Nanoparticles. *J. Phys. Chem. C* **2007**, *111*, 14925–14931. [[CrossRef](#)]
5. Kavan, L.; Kalbáč, M.; Zukalová, M.; Exnar, I.; Lorenzen, V.; Nesper, R.; Graetzel, M. Lithium Storage in Nanostructured TiO_2 Made by Hydrothermal Growth. *Chem. Mater.* **2004**, *16*, 477–485. [[CrossRef](#)]
6. Augustyn, V.; Simon, P.; Dunn, B. Pseudocapacitive Oxide Materials for High-Rate Electrochemical Energy Storage. *Energy Environ. Sci.* **2014**, *7*, 1597. [[CrossRef](#)]
7. Brousse, T.; Bélanger, D.; Long, J.W. To Be or Not to Be Pseudocapacitive? *J. Electrochem. Soc.* **2015**, *162*, A5185–A5189. [[CrossRef](#)]
8. Li, J.; Tang, Z.; Zhang, Z. Layered Hydrogen Titanate Nanowires with Novel Lithium Intercalation Properties. *Chem. Mater.* **2005**, *17*, 5848–5855. [[CrossRef](#)]
9. Li, J.; Tang, Z.; Zhang, Z. H-Titanate Nanotube: A Novel Lithium Intercalation Host with Large Capacity and High Rate Capability. *Electrochem. Commun.* **2005**, *7*, 62–67. [[CrossRef](#)]
10. Wei, M.; Wei, K.; Ichihara, M.; Zhou, H. High Rate Performances of Hydrogen Titanate Nanowires Electrodes. *Electrochem. Commun.* **2008**, *10*, 1164–1167. [[CrossRef](#)]
11. Zhu, G.-N.; Wang, C.-X.; Xia, Y.-Y. Structural Transformation of Layered Hydrogen Trititanate ($\text{H}_2\text{Ti}_3\text{O}_7$) to TiO_2 (B) and Its Electrochemical Profile for Lithium-Ion Intercalation. *J. Power Sources* **2011**, *196*, 2848–2853. [[CrossRef](#)]
12. Wang, Y.; Hong, Z.; Wei, M.; Xia, Y. Layered $\text{H}_2\text{Ti}_6\text{O}_{13}$ -Nanowires: A New Promising Pseudocapacitive Material in Non-Aqueous Electrolyte. *Adv. Funct. Mater.* **2012**, *22*, 5185–5193. [[CrossRef](#)]
13. Ohzuku, T.; Sawai, K.; Hirai, T. Electrochemistry of L-Niobium Pentoxide a Lithium/Non-Aqueous Cell. *J. Power Sources* **1987**, *19*, 287–299. [[CrossRef](#)]
14. Brezesinski, K.; Wang, J.; Haetge, J.; Reitz, C.; Steinmueller, S.O.; Tolbert, S.H.; Smarsly, B.M.; Dunn, B.; Brezesinski, T. Pseudocapacitive Contributions to Charge Storage in Highly Ordered Mesoporous Group V Transition Metal Oxides with Iso-Oriented Layered Nanocrystalline Domains. *J. Am. Chem. Soc.* **2010**, *132*, 6982–6990. [[CrossRef](#)] [[PubMed](#)]
15. Kim, J.W.; Augustyn, V.; Dunn, B. The Effect of Crystallinity on the Rapid Pseudocapacitive Response of Nb_2O_5 . *Adv. Energy Mater.* **2012**, *2*, 141–148. [[CrossRef](#)]

16. Augustyn, V.; Come, J.; Lowe, M.A.; Kim, J.W.; Taberna, P.-L.; Tolbert, S.H.; Abruña, H.D.; Simon, P.; Dunn, B. High-Rate Electrochemical Energy Storage through Li⁺ Intercalation Pseudocapacitance. *Nat. Mater.* **2013**, *12*, 518–522. [[CrossRef](#)]
17. Zheng, H.; Ou, J.Z.; Strano, M.S.; Kaner, R.B.; Mitchell, A.; Kalantar-zadeh, K. Nanostructured Tungsten Oxide—Properties, Synthesis, and Applications. *Adv. Funct. Mater.* **2011**, *21*, 2175–2196. [[CrossRef](#)]
18. Granqvist, C.G. Electrochromic Materials: Microstructure, Electronic Bands, and Optical Properties. *Appl. Phys. A* **1993**, *57*, 3–12. [[CrossRef](#)]
19. Gao, T.; Jelle, B.P. Visible-Light-Driven Photochromism of Hexagonal Sodium Tungsten Bronze Nanorods. *J. Phys. Chem. C* **2013**, *117*, 13753–13761. [[CrossRef](#)]
20. Gao, T.; Jelle, B.P. Electrochromism of Hexagonal Sodium Tungsten Bronze Nanorods. *Sol. Energy Mater. Sol. Cells.* **2018**, *177*, 3–8. [[CrossRef](#)]
21. Besnardiere, J.; Ma, B.; Torres-Pardo, A.; Wallez, G.; Kabbour, H.; González-Calbet, J.M.; Von Bardeleben, H.J.; Fleury, B.; Buissette, V.; Sanchez, C.; et al. Structure and Electrochromism of Two-Dimensional Octahedral Molecular Sieve h'-WO₃. *Nat. Commun.* **2019**, *10*, 327. [[CrossRef](#)] [[PubMed](#)]
22. Shinde, P.A.; Jun, S.C. Review on Recent Progress in the Development of Tungsten Oxide Based Electrodes for Electrochemical Energy Storage. *ChemSusChem* **2020**, *13*, 11–38. [[CrossRef](#)] [[PubMed](#)]
23. Mitchell, J.B.; Lo, W.C.; Genc, A.; LeBeau, J.; Augustyn, V. Transition from Battery to Pseudocapacitor Behavior via Structural Water in Tungsten Oxide. *Chem. Mater.* **2017**, *29*, 3928–3937. [[CrossRef](#)]
24. Mitchell, J.B.; Geise, N.R.; Paterson, A.R.; Osti, N.C.; Sun, Y.; Fleischmann, S.; Zhang, R.; Madsen, L.A.; Toney, M.F.; Jiang, D.; et al. Confined Interlayer Water Promotes Structural Stability for High-Rate Electrochemical Proton Intercalation in Tungsten Oxide Hydrates. *ACS Energy Lett.* **2019**, *4*, 2805–2812. [[CrossRef](#)]
25. Magnéli, A. Tungsten Bronzes Containing Six-Membered Rings of WO₆ Octahedra. *Nature* **1952**, *169*, 791–792. [[CrossRef](#)]
26. Gerand, B.; Nowogrocki, G.; Guenot, J.; Figlarz, M. Structural Study of a New Hexagonal Form of Tungsten Trioxide. *J. Solid State Chem.* **1979**, *29*, 429–434. [[CrossRef](#)]
27. Gerand, B.; Nowogrocki, G.; Figlarz, M. A New Tungsten Trioxide Hydrate, WO₃·1/3H₂O: Preparation, Characterization, and Crystallographic Study. *J. Solid State Chem.* **1981**, *38*, 312–320. [[CrossRef](#)]
28. Reis, K.P.; Ramanan, A.; Whittingham, M.S. Hydrothermal Synthesis of Sodium Tungstates. *Chem. Mater.* **1990**, *2*, 219–221. [[CrossRef](#)]
29. Reis, K.P.; Prince, E.; Whittingham, M.S. Rietveld Analysis of Sodium Tungstate Hydrate Na_xWO₃+x/2.YH₂O, Which Has the Hexagonal Tungsten Bronze Structure. *Chem. Mater.* **1992**, *4*, 307–312. [[CrossRef](#)]
30. Reis, K.P.; Ramanan, A.; Whittingham, M.S. Synthesis of Novel Compounds with the Pyrochlore and Hexagonal Tungsten Bronze Structures. *J. Solid State Chem.* **1992**, *96*, 31–47. [[CrossRef](#)]
31. Kumagai, N.; Kumagai, N.; Tanno, K. Electrochemical and Structural Characteristics of Tungstic Acids as Cathode Materials for Lithium Batteries. *Appl. Phys. A* **1989**, *49*, 83–89. [[CrossRef](#)]
32. Kumagai, N.; Matsuura, Y.; Kumagai, N.; Tanno, K. Kinetic and Structural Studies of the Electrochemical Insertion of Lithium into Hexagonal-Type x(A₂O) WO₃. *J. Electrochem. Soc.* **1992**, *139*, 3553–3558. [[CrossRef](#)]
33. Pereira-Ramos, J.-P. Electrochemical Properties of Cathodic Materials Synthesized by Low-Temperature Techniques. *J. Power Sources* **1995**, *54*, 120–126. [[CrossRef](#)]
34. Kumagai, N.; Kumagai, N.; Umetzu, Y.; Tanno, K.; Pereira-Ramos, J.P. Synthesis of Hexagonal Form of Tungsten Trioxide and Electrochemical Lithium Insertion into the Trioxide. *Solid State Ion.* **1996**, *86–88*, 1443–1449. [[CrossRef](#)]
35. Gu, Z.; Ma, Y.; Zhai, T.; Gao, B.; Yang, W.; Yao, J. A Simple Hydrothermal Method for the Large-Scale Synthesis of Single-Crystal Potassium Tungsten Bronze Nanowires. *Chem. Eur. J* **2006**, *12*, 7717–7723. [[CrossRef](#)]
36. Wang, J.; Khoo, E.; Lee, P.S.; Ma, J. Synthesis, Assembly, and Electrochromic Properties of Uniform Crystalline WO₃ Nanorods. *J. Phys. Chem. C* **2008**, *112*, 14306–14312. [[CrossRef](#)]
37. Lee, J.-S.; Liu, H.-C.; Peng, G.-D.; Tseng, Y. Facile Synthesis and Structure Characterization of Hexagonal Tungsten Bronzes Crystals. *J. Cryst. Growth* **2017**, *465*, 27–33. [[CrossRef](#)]
38. Miao, B.; Zeng, W.; Hussain, S.; Mei, Q.; Xu, S.; Zhang, H.; Li, Y.; Li, T. Large Scale Hydrothermal Synthesis of Monodisperse Hexagonal WO₃ Nanowire and the Growth Mechanism. *Mater. Lett.* **2015**, *147*, 12–15. [[CrossRef](#)]
39. Petříček, V.; Dušek, M.; Palatinus, L. Crystallographic Computing System JANA2006: General Features. *Z. Kristallogr. Krist.* **2014**, *229*, 345–352. [[CrossRef](#)]
40. Brousse, T.; Taberna, P.-L.; Crosnier, O.; Dugas, R.; Guillemet, P.; Scudeller, Y.; Zhou, Y.; Favier, F.; Bélanger, D.; Simon, P. Long-Term Cycling Behavior of Asymmetric Activated Carbon/MnO₂ Aqueous Electrochemical Supercapacitor. *J. Power Sources* **2007**, *173*, 633–641. [[CrossRef](#)]
41. Gogotsi, Y.; Simon, P. True Performance Metrics in Electrochemical Energy Storage. *Science* **2011**, *334*, 917–918. [[CrossRef](#)]
42. Briois, V.; La Fontaine, C.; Belin, S.; Barthe, L.; Moreno, T.; Pinty, V.; Carcy, A.; Girardot, R.; Fonda, E. ROCK: The New Quick-EXAFS Beamline at SOLEIL. *J. Phys. Conf. Ser.* **2016**, *712*, 012149. [[CrossRef](#)]
43. Goubard-Bretesché, N.; Crosnier, O.; Douard, C.; Iadecola, A.; Retoux, R.; Payen, C.; Doublet, M.; Kisu, K.; Iwama, E.; Naoi, K.; et al. Unveiling Pseudocapacitive Charge Storage Behavior in FeWO₄ Electrode Material by *Operando* X-ray Absorption Spectroscopy. *Small* **2020**, *16*, 2002855. [[CrossRef](#)]

44. Fleischmann, S.; Shao, H.; Taberna, P.-L.; Rozier, P.; Simon, P. Electrochemically Induced Deformation Determines the Rate of Lithium Intercalation in Bulk TiS_2 . *ACS Energy Lett.* **2021**, *6*, 4173–4178. [[CrossRef](#)]
45. Trasatti, S. Effect of the Nature of the Metal on the Dielectric Properties of Polar Liquids at the Interface with Electrodes. A Phenomenological Approach. *J. Electroanal. Chem. Interfacial Electrochem.* **1981**, *123*, 121–139. [[CrossRef](#)]
46. Ribnick, A.S.; Post, B.; Banks, E. Phase Transitions in Sodium Tungsten Bronzes. In *Nonstoichiometric Compounds; Advances in Chemistry*; American Chemical Society: Washington, DC, USA, 1963; Volume 39, ISBN 978-0-8412-0040-1.
47. Dickens, P.G.; Whittingham, M.S. The Tungsten Bronzes and Related Compounds. *Q. Rev. Chem. Soc.* **1968**, *22*, 30. [[CrossRef](#)]
48. Wu, Y.-C.; Taberna, P.-L.; Simon, P. Tracking Ionic Fluxes in Porous Carbon Electrodes from Aqueous Electrolyte Mixture at Various PH. *Electrochem. Commun.* **2018**, *93*, 119–122. [[CrossRef](#)]
49. Shao, H.; Xu, K.; Wu, Y.-C.; Iadecola, A.; Liu, L.; Ma, H.; Qu, L.; Raymundo-Piñero, E.; Zhu, J.; Lin, Z.; et al. Unraveling the Charge Storage Mechanism of $\text{Ti}_3\text{C}_2\text{T}_x$ MXene Electrode in Acidic Electrolyte. *ACS Energy Lett.* **2020**, *5*, 2873–2880. [[CrossRef](#)]
50. Darwiche, A.; Murgia, F.; Fehse, M.; Mahmoud, A.; Iadecola, A.; Belin, S.; La Fontaine, C.; Briois, V.; Hermann, R.P.; Fraise, B.; et al. *Operando X-ray Absorption Spectroscopy Applied to Battery Materials at ICGM: The Challenging Case of BiSb's Sodiation.* *Energy Storage Mater.* **2019**, *21*, 1–13. [[CrossRef](#)]
51. Robert, K.; Stiévenard, D.; Deresmes, D.; Douard, C.; Iadecola, A.; Troadec, D.; Simon, P.; Nuns, N.; Marinova, M.; Huvé, M.; et al. Novel Insights into the Charge Storage Mechanism in Pseudocapacitive Vanadium Nitride Thick Films for High-Performance on-Chip Micro-Supercapacitors. *Energy Environ. Sci.* **2020**, *13*, 949–957. [[CrossRef](#)]
52. Khyzhun, O.Y. XPS, XES and XAS Studies of the Electronic Structure of Tungsten Oxides. *J. Alloys Compd.* **2000**, *305*, 1–6. [[CrossRef](#)]
53. Pauporté, T.; Soldo-Olivier, Y.; Faure, R. In-situ X-ray Absorption Spectroscopy Study of Lithium Insertion into Sputtered WO_3 Thin Films. *J. Electroanal. Chem.* **2004**, *562*, 111–116. [[CrossRef](#)]
54. Nam, K.-W.; Kim, M.G.; Kim, K.-B. In-situ Mn K-Edge X-ray Absorption Spectroscopy Studies of Electrodeposited Manganese Oxide Films for Electrochemical Capacitors. *J. Phys. Chem. C* **2007**, *111*, 749–758. [[CrossRef](#)]
55. Chang, J.-K.; Lee, M.-T.; Tsai, W.-T. In-situ Mn K-Edge X-ray Absorption Spectroscopic Studies of Anodically Deposited Manganese Oxide with Relevance to Supercapacitor Applications. *J. Power Sources* **2007**, *166*, 590–594. [[CrossRef](#)]
56. Kuo, S.-L.; Lee, J.-F.; Wu, N.-L. Study on Pseudocapacitance Mechanism of Aqueous MnFe_2O_4 Supercapacitor. *J. Electrochem. Soc.* **2006**, *154*, A34–A38. [[CrossRef](#)]
57. Fehse, M.; Iadecola, A.; Sougrati, M.T.; Conti, P.; Giorgetti, M.; Stievano, L. Applying Chemometrics to Study Battery Materials: Towards the Comprehensive Analysis of Complex *Operando* Datasets. *Energy Storage Mater.* **2019**, *18*, 328–337. [[CrossRef](#)]
58. Suo, L.; Borodin, O.; Gao, T.; Olguin, M.; Ho, J.; Fan, X.; Luo, C.; Wang, C.; Xu, K. “Water-in-Salt” Electrolyte Enables High-Voltage Aqueous Lithium-Ion Chemistries. *Science* **2015**, *350*, 938–943. [[CrossRef](#)]
59. Ohtaki, H.; Radnai, T. Structure and Dynamics of Hydrated Ions. *Chem. Rev.* **1993**, *93*, 1157–1204. [[CrossRef](#)]
60. Rempe, S.B.; Pratt, L.R.; Hummer, G.; Kress, J.D.; Martin, R.L.; Redondo, A. The Hydration Number of Li^+ in Liquid Water. *J. Am. Chem. Soc.* **2000**, *122*, 966–967. [[CrossRef](#)]
61. Marcus, Y. Effect of Ions on the Structure of Water: Structure Making and Breaking. *Chem. Rev.* **2009**, *109*, 1346–1370. [[CrossRef](#)]
62. Järvinen, M. Application of Symmetrized Harmonics Expansion to Correction of the Preferred Orientation Effect. *J. Appl. Crystallogr.* **1993**, *26*, 525–531. [[CrossRef](#)]
63. Slade, R.C.T.; West, B.C.; Hall, G.P. Chemical and Electrochemical Mixed Alkali Metal Insertion Chemistry of the Hexagonal Tungsten Trioxide Framework. *Solid State Ion.* **1989**, *32–33*, 154–161. [[CrossRef](#)]
64. Oi, J.; Kishimoto, A.; Kudo, T.; Hiratani, M. Hexagonal Tungsten Trioxide Obtained from Peroxo-Polytungstate and Reversible Lithium Electro-Intercalation into Its Framework. *J. Solid State Chem.* **1992**, *96*, 13–19. [[CrossRef](#)]
65. Hoffmann, R.; Hoppe, R. Zwei neue Ordnungs-Varianten des NaCl-Typs: Li_4MoO_5 und Li_4WO_5 . *Z. Anorg. Allg. Chem.* **1989**, *573*, 157–169. [[CrossRef](#)]
66. Fourquet, J.L.; Le Bail, A.; Gillet, P.A. LiNbWO_6 : Crystal Structure of Its Two Allotropic Forms. *Mater. Res. Bull.* **1988**, *23*, 1163–1170. [[CrossRef](#)]
67. Pralong, V.; Venkatesh, G.; Malo, S.; Caignaert, V.; Baies, R.; Raveau, B. Electrochemical Synthesis of a Lithium-Rich Rock-Salt-Type Oxide $\text{Li}_5\text{W}_2\text{O}_7$ with Reversible Deintercalation Properties. *Inorg. Chem.* **2014**, *53*, 522–527. [[CrossRef](#)]
68. Tsai, W.-Y. Ion Adsorption in Porous Carbon: From Fundamental Studies to Supercapacitor Applications. Ph.D. Thesis, Université Toulouse III-Paul Sabatier, Toulouse, France, 2015.

Disclaimer/Publisher’s Note: The statements, opinions and data contained in all publications are solely those of the individual author(s) and contributor(s) and not of MDPI and/or the editor(s). MDPI and/or the editor(s) disclaim responsibility for any injury to people or property resulting from any ideas, methods, instructions or products referred to in the content.